10-23-2023

Turn-on Rhodamine Glycoconjugates Enable Real-Time GLUT Activity Monitoring in Live Cells and In Vivo

Monica M.S. Nyansa
Michigan Technological University, mnyansa@mtu.edu

Adelina Oronova
Michigan Technological University, aoronova@mtu.edu

Nazar Gora
Michigan Technological University, ngora@mtu.edu

Micaela Rayne Geborkoff
Michigan Technological University, mrgebork@mtu.edu

Nathan Ostlund
Michigan Technological University, nrostlun@mtu.edu

See next page for additional authors

Recommended Citation

Nyansa, M., Oronova, A., Gora, N., Geborkoff, M. R., Ostlund, N., Fritz, D., Werner, T., & Tanasova, M. (2023). Turn-on Rhodamine Glycoconjugates Enable Real-Time GLUT Activity Monitoring in Live Cells and In Vivo. *Chemical & biomedical imaging, 1*(7), 637-647. http://doi.org/10.1021/cbmi.3c00063
Retrieved from: https://digitalcommons.mtu.edu/michigantech-p2/237

ACS Partner Journal

CHEMICAL & BIOMEDICAL IMAGING

pubs.acs.org/ChemBioImaging

Article

Turn-on Rhodamine Glycoconjugates Enable Real-Time GLUT Activity Monitoring in Live Cells and In Vivo

Monica Mame Soma Nyansa,[‖] Adelina Oronova,[‖] Nazar Gora, Micaela Rayne Geborkoff, Nathan Randal Ostlund, Delaney Raine Fritz, Thomas Werner, and Marina Tanasova*

Cite This: *Chem. Biomed. Imaging* 2023, 1, 637−647

Read Online

ACCESS | Metrics & More | Article Recommendations | Supporting Information

ABSTRACT: The direct relationship between facilitative glucose transporters (GLUTs) and metabolic diseases opens new avenues for sensing metabolic deregulations and drives the development of molecular probes for GLUT-targeted detection of metabolic diseases. Radiotracer-based molecular imaging probes have been effectively utilized in reporting alterations in sugar uptake as an indication of metabolic deregulations, cancer development, or inflammation. Progress in developing fluorophore-based tools facilitated GLUT-specific analyses using more accessible fluorescence-based instrumentation. However, restrictions on the emission range of fluorophores and the requirement for substantial post-treatments to reduce background fluorescence have brought to light the critical directions for improvement of the technology for broader use in screening applications. Here we present turn-on GLUT activity reporters activated upon cells' internalization. We demonstrate a specific delivery of a sizable rhodamine B fluorophore through GLUT5 and showcase a stringent requirement in conjugate structure for maintaining a GLUT-specific uptake. With the turn-on GLUT probes, we demonstrate the feasibility of high-throughput fluorescence microscopy and flow cytometry-based GLUT activity screening in live cells and the probes' applicability for assessing sugar uptake alterations *in vivo*.

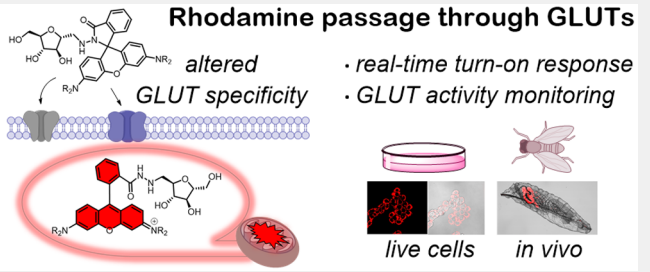

KEYWORDS: *carbohydrates, sugar transporters, GLUT, glycoconjugates, turn-on fluorescence, high-throughput analysis*

INTRODUCTION

Detecting cellular alterations is a global approach that has been applied to the identification of disorders and diseases. Alterations in cellular metabolic processes were found to change the levels of sugar uptake, highlighting the vital role of sugar transport in multiple conditions, including hypertension, obesity, type 2 diabetes, and cancer.[1−4] Accordingly, GLUT expression and activity deregulation has been linked to various metabolic disorders, including cancer.

The higher energy demands of cancer cells prompted the development of a metabolism-driven approach to cancer detection and treatment. A specific focus on targeting GLUTs yielded glucose-based radiotracers for positron emission tomography (PET) imaging.[5] New directions toward cancer diagnosis have focused on identifying more cancer-specific targets. Among those, the uptake of fructose has unveiled significant cancer relevance, with the activity of the fructose-specific transporter GLUT5 particularly linked to cancer development, progression, and metastasis.[6] Respectively, GLUT5 targeting has been explored using fructose-based radiotracers for *in vivo* cancer imaging,[7−10] with a superiority over glucose performance of tracers in animal models yet to be achieved. GLUT5 targeting for drug delivery has achieved limited success and reflected the stringent substrate requirements of the transporter.[11] Some success in biomedical applications has been reported with the GLUT5 inhibition approach, with a GLUT5-specific inhibitor shown to potentiate the activity of conventional anticancer drugs.[12]

The broad relevance of GLUT5 for a variety of metabolic disorders highlights the need for effective activity reporters. Some progress has been reported in GLUT5-targeting with analytical probes allowing fluorescence-based GLUT5 activity analysis in cell cultures.[13−19] Molecular probes developed to date to analyze GLUT activity encompass small fluorophores (e.g., NBD, coumarins) and are delivered through the GLUT transporters in the form of a glycoconjugate. While allowing to shift from the use of radiotracer-based probes in analytical settings, the background fluorescence of these inherently fluorescent compounds (or "always-on" fluorophores) challenges their broader application, requiring proper controls for data interpretation, washing steps, or sample-driven optimization of probe concentration.[20] Limitations in the applicability of "always-on" fluorophores necessitate the development of

Received: May 25, 2023
Revised: August 14, 2023
Accepted: August 16, 2023
Published: September 1, 2023

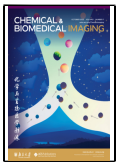

activatable (e.g., turn-on) fluorescent probes for GLUT activity analysis.

In this paper, we demonstrate the proof-of-concept for GLUT-dependent delivery of turn-on fluorophores and report the first GLUT5-specific rhodamine-based "turn-on" fluorescent probe. We show that despite the larger size, the turn-on rhodamine-based dyes can effectively pass through GLUTs in the form of a glycoconjugate. The GLUT specificity appears to alter with rhodamine substitution, with rhodamine B conjugate showing specific uptake through GLUT5. The turn-on property of the presented GLUT probes allows for comparative analysis of transport activity, inhibitor screening in live cells, and visualization of changes in GLUT activity *in vivo*.

RESULTS AND DISCUSSION

Probe Design, Synthesis, and Properties

Xanthene scaffold-based fluorophores are among the most used turn-on fluorophores. The compact structure of the xanthene moiety adds stability, decreases molecular weight, and promotes moderate hydrophilicity.[21] The rhodamine scaffold (Scheme 1) bears amino substituents at positions 3 and 6 of the xanthene and provides fluorescence emission at high wavelengths, high quantum yield, and high absorption coefficient. Functionalization of xanthene scaffold at the pyran moiety with a spirocyclic lactone allowed for switching fluorescence off-on depending on the external environment. The spirocyclic form of rhodamine B has been shown to exhibit pH-dependent fluorescence and turn on the fluorescence under acidic conditions (Figure S1).[22] In polar solvents, the conjugation-prone rhodamine B scaffold is suggested to equilibrate with the fluorescent ring-opened zwitterion form. This form is further stabilized by the acidic pH or metal ions, resulting in fluorescence and absorbance enhancement and enabling a broad range of applications in live cell imaging.[21] In this study, we have assessed the feasibility of the specific delivery of a rhodamine dye through the cancer-relevant fructose-specific transporter GLUT5 with the goal of generating efficient molecular tools for real-time GLUT5 activity analysis.

For conjugate design, we selected rhodamine B and rhodamine-azetidine.[23] For the synthesis of glycoconjugates, we envisioned using the hydrazide derivatives of rhodamine dyes that provide a primary amine as a convenient site for glycoconjugation. 2,5-Anhydro-D-mannitol (Man, 2,5-AM) has been shown to target specifically the GLUT5 transporter and has a higher affinity for GLUT5 than fructose.[13,14] Subsequently, mannitol conjugates of rhodamine B and rhodamine-azetidine were synthesized (Scheme 1) through reductive amination between the aldehyde of the sugar (**3**) and the primary amino group of rhodamine hydrazine. The synthesis proceeded with moderate efficiency, yielding ManRho-B and ManRho-Az conjugates in 20−25% (Scheme 1). Rhodamine-azetidine was synthesized from fluorescein following established procedures.[24,25] The purity of the final products was confirmed by HRMS, ^{1}H NMR, and ^{13}C NMR (see SI for details).

Scheme 1. Synthetic Routes to ManRho-B and ManRho-Az Glycoconjugates (see SI for experimental details)

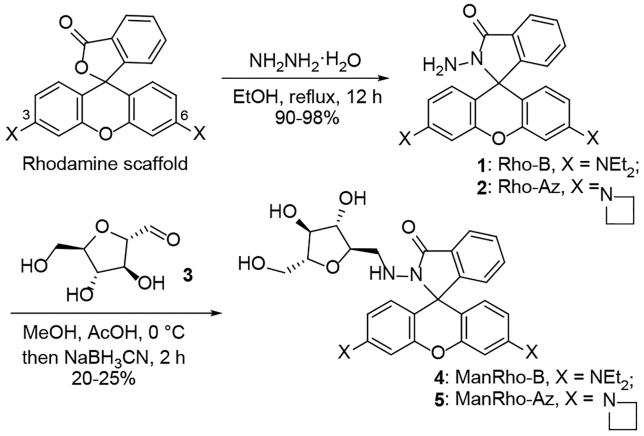

The pH dependence of probe absorbance and fluorescence was evaluated by UV−vis and fluorescence spectroscopy, using a series of standard pH buffers (pH 0.8−10). For both probes, fluorescence was low at the neutral or basic pH and enhanced at pH 6 or below (Figure S2A,B). The conjugation of the chromophore in an acidic environment was also supported by the enhancement in the absorbance (Figure S2C,D). The pK_a values for ManRho conjugates were determined by monitoring the change in the fluorescence of probes (Figure S2E,F). The equilibrium between the conjugate base and conjugate acid was observed at pH < 6, reflecting the acid-catalyzed transition between the nonfluorescent spirolactam and a fluorescent ring-opened amide. The pK_a values of 5.7 for ManRho-B and 4.6 for ManRho-Az were derived using GraphPad Prism 9.4.1.

Changes in Fluorophore Structure Impact Uptake Efficiency and Retention in Live Cells

With the turn-on fluorescence for probes occurring at pH < 6, we moved to the probe analysis in live cells. For this part, breast adenocarcinoma MCF7 cells expressing GLUT5 and other GLUTs[14] were treated with different probe concentrations. Probe solutions were prepared in the complete RPMI cell culture medium, and cells were incubated for 15 min to assess the contribution of facilitative probe uptake. After 15 min of incubation at 37 °C, the cells were imaged by confocal microscopy after the removal of the probe ("wash" conditions). The apparent concentration-dependent red fluorescence was observed in cells for both probes (Figure 1A) with no

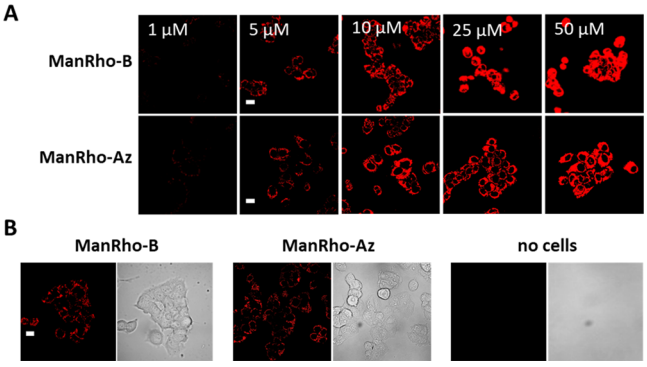

Figure 1. Fluorescence of ManRho-B and ManRho-Az in MCF7 cells after cell wash (A) or without cell wash (B). For B, cells were treated with 2 μM probe. For A and B, cells were treated for 15 min at 37 °C. Images were taken using a confocal microscope, 60× objective, 14% laser intensity, Alexa Fluor 568 filter (exc 559 nm/em 603 nm). The scale bar is 20 μm.

https://doi.org/10.1021/cbmi.3c00063
Chem. Biomed. Imaging 2023, 1, 637−647

fluorescence detectable in the background. To assess the background fluorescence of probes, MCF7 cells were incubated at 37 °C for 15 min with 2 μM probe solutions in the complete culture media and imaged directly after incubation without cell wash ("no-wash" conditions). Despite the presence of probes in the culture media, the probe-induced fluorescence was detectable only in cells (Figure 1B), indicating the turn-on fluorescence mechanism upon probe internalization by cells. Respectively, no fluorescence was visible in dishes containing probes but not cells. The overall probe-induced fluorescence levels between "wash" and "no-wash" conditions were comparable (Figure S3). The levels of uptake were similar for the probe solutions in DPBS or RPMI (Figure S4), highlighting the efficient competition between a rhodamine glycoconjugate with culture medium nutrients for the uptake.

As probes can be imaged without any post-treatments, direct monitoring of probe-induced fluorescence over time became feasible. Hence, we assessed the probe accumulation over time in MCF7 cells at room temperature without an incubation period. For this part, the probe was directly added to the cell-containing confocal dish and imaged over 60 min with a confocal microscope ("no wash" conditions). The corresponding fluorescence images were quantified using ImageJ to derive probe-induced fluorescence as the corrected total cell fluorescence per cell area (CTCF/Area): CTCF = (integrated density − (area of selected cell × mean fluorescence of background readings)/area of the selected cell. We have found that two probes developed fluorescence with different rates (Figure S5). While fluorescence from ManRho-B was observable at 10 min, it required 20 min for ManRho-Az to develop a well-detectable signal at the same imaging setting. After 25 min, the fluorescence signal equilibrated for ManRho-B. Saturation of the uptake reflected the lack of probe phosphorylation and the stabilization of the "turn-on" state for the fluorophore. For ManRho-Az, the stabilization of the signal was observed from between 25 and 40 min, with further incubation time leading to the enhancement in the probe-produced fluorescence. Overall, both probes were established to have a time-dependent uptake that equilibrates within 20−40 min, providing an interval for measuring the relative activity of the transport. The probe uptake levels were not altered by postincubation treatment (wash vs no-wash, Figure S5), reflecting the lack of fluorescence contribution from the probe in the media.

The variances in time-dependent fluorescence between the two probes could be attributed to the differences in probe uptake efficiencies. To quantify the probe uptake efficiencies, the concentration dependence of the uptake was used. We observed that with the selected 14% laser intensity, signal saturation was observed at probe concentrations >20 μM (probe uptake evaluated during the active uptake time) (Figures S6 and S7). In contrast, no saturation could be observed at 5% and 3% laser intensity for up to 50 μM probe concentration.

The data of probes' uptake at different laser intensities have identified the uptake-independent fluorescence signal saturation necessitating the application of alternative fluorescence detection technologies in probe uptake analysis at higher concentrations. To facilitate fluorescence measurements at higher probe concentrations, we analyzed the probe uptake using flow cytometry. The resulting data reflected significant differences in the uptake efficiencies of probes. Thus, while ManRho-B uptake saturated between 50 and 100 μM concentrations (Figure S6C), the uptake of ManRho-Az saturated at concentrations >200 μM (Figure S7C). The Michaelis−Menten kinetic analysis (GraphPad Prism 9.4.1) of probe uptake derived from flow settings resulted in $K_m \sim 37$ μM for ManRho-B and $K_m \sim 164$ μM for ManRho-Az, reflecting a higher efficiency of ManRho-B uptake and showcasing a significant impact of the subtle structural differences on probe uptake properties.

Differences between the two probes were also detected for their in-cell retention. Here, we monitored fluorescence amassed in the fresh dye-free culture medium supplemented to MCF7 cells post-treatment with probes, and analyzed samples were collected in 5 and 20 min (Figure S8) postincubation. Earlier reports highlighted the ability of positively charged rhodamines to specifically stain mitochondria at physiological pH values.[20] The localization in lysosomes was also reported for spirolactam derivatives of rhodamines.[21] Hence, we evaluated probe localization within mitochondria and lysosomes using corresponding organelle-specific dyes. Cotreatment of MCF7 cells with ManRho-dye mixture followed by imaging of fluorophores using nonoverlapping fluorescence filters reflected major differences in organelle-specific accumulation between probes. The colocalization studies with the mitochondrial dye MitoView (Figure 2A)

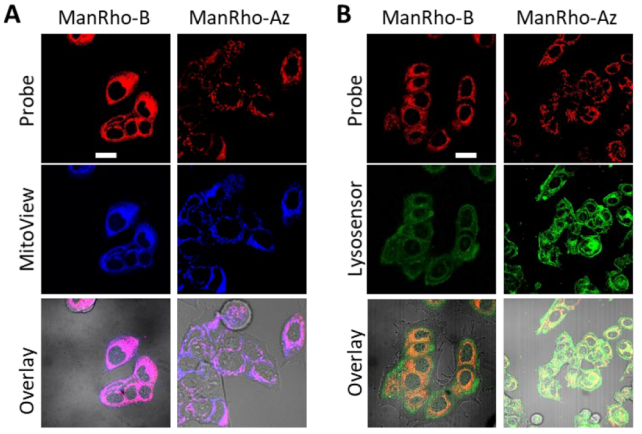

Figure 2. Localization of ManRho-B and ManRho-Az. (A) Colocalization of probes (2 μM, red) with MitoView (1 μM, blue). (B) Colocalization of probes (2 μM, red) with Lysosensor Green (1 μM, green). Cells were treated with the probe/dye mixture for 15 min at 37 °C. Images acquired after cell wash using confocal microscope and a 100× objective. Alexa Fluor 568 filter (exc 559 nm/em 603 nm) for ManRho-B and ManRho-Az, DAPI (exc 405 nm/em 461 nm) for MitoView, and Alexa Fluor 488 filter (exc 488 nm/em 520 nm) for Lysosensor Green. The scale bar is 20 μm.

showed a significant mitochondrial accumulation for ManRho-B despite the presence of a sugar moiety (Pearson's correlation coefficient: (r) = 0.93). In contrast, mitochondrial accumulation of ManRho-Az was lower ((r) = 0.79). The lysosomal accumulation evaluated by coincubation with Lysosensor Green was weak for both probes ((r) = 0.52 and 0.35 for ManRho-B and -Az, respectively, Figure 2B). Hence, mitochondrial accumulation appears to contribute to the saturation of the uptake and retention of ManRho-B in cells. On the other hand, the cytosolic accumulation of the ManRho-Az putatively allows for a more effective internalization of the probe inside the cell, albeit providing limited cellular retention.

https://doi.org/10.1021/cbmi.3c00063
Chem. Biomed. Imaging 2023, 1, 637−647

The cytotoxicity of probes was assessed in MCF7 cells using an MTS assay. The analysis showed that 1−10 μM concentrations of probes have no impact on cell viability for up to 24 h (Figure S9). Considering the <1 h time frame for probe-based fluorescence analyses, the tolerance of cells to probe impact at low concentrations and short incubation time allows for their safe usage as analytical tools.

ManRho-B and ManRho-Az Reflect Stringent Structural Requirements for GLUT5 Specificity

With glycoconjugation directing small molecules toward GLUTs,[5] and 2,5-AM-conjugation enabling GLUT5-mediated uptake of fluorophores,[13,14,16,26] we moved toward assessing the GLUT participation in the uptake of rhodamine conjugates. For this part, we have used the established link between GLUT-mediated uptake and cellular metabolism, as diminished metabolism was shown to reduce GLUT activity.[27] Decreasing the metabolic activity of cells is achievable by lowering the cell incubation temperature.[15,27] Accordingly, the probe uptake was evaluated in MCF7 cells preincubated at 4 °C vs 37 °C. The temperature-induced alterations in cell metabolism resulted in abolished probe-induced fluorescence in the 4 °C samples (Figure 3), reflecting metabolism-coupled probe uptake.

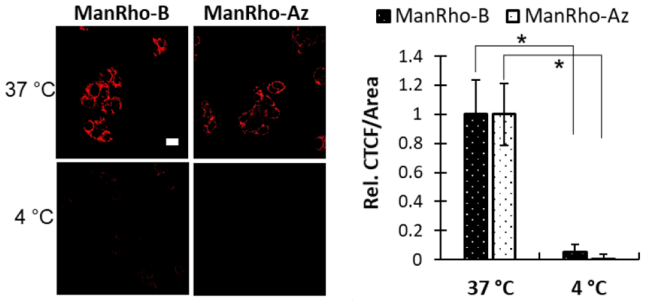

Figure 3. Impact of metabolic activity on probe uptake. (A) Fluorescence images of probe-treated (2 μM) MCF7 cells preconditioned at 37 °C vs 4 °C. Images were acquired using a confocal microscope, 60× objective, and Alexa Fluor 568 filter (exc 559 nm/em 603 nm) at the same laser intensity and exposure time. The scale bar is 20 μm. (B) Relative differences in probe uptake at 37 °C vs 4 °C. Data derived through quantification of fluorescence in A using ImageJ as CTCF/area: CTCF = (integrated density − (area of selected cell × mean fluorescence of background readings)/area of the selected cell. Probe uptake levels at 37 °C vs 4 °C were corrected by the corresponding value obtained for 37 °C to represent rel CTCF/area. Error bars represent the relative standard deviation. Statistically significant differences were established through a two-tailed *t*-test: *p < 0.05.

While the loss in probe uptake at 4 °C indicated the metabolism-coupled uptake, the difference in probe uptake efficiencies suggested dissimilar uptake paths for the two rhodamine conjugates. To confirm the GLUT involvement and establish a specific GLUT path for each probe, we assessed probe uptake in the presence of GLUT substrates and inhibitors. Each probe was introduced in combination with the competing substrate in the complete culture medium, and the changes in the total probe uptake as compared to the control (probe without competitor) were measured. Competition with cytochalasin B (CyB) was used to delineate the involvement of nonspecific glucose and fructose GLUTs (1−4, 6, 10, and 12).[28,29] Competition with fructose was used to establish the involvement of fructose GLUTs. To assess GLUT5 contribution to the probes' uptake, competition with a high-affinity GLUT5-specific ligand MSNBA was utilized.[30] To distinguish the involvement of nonspecific GLUT2, a high-affinity GLUT2 substrate glucosamine (GluAm, K_m ∼ 0.8 mM[31]) was used. The probe uptake was recorded using a confocal microscope, and the corresponding fluorescence images (Figure S10) were quantified using ImageJ to derive probe-induced fluorescence as CTCF/area.

Despite the structural similarities between ManRho-B and ManRho-Az, significant differences in probe responses to inhibitors have been identified (Figures 4A and S10).

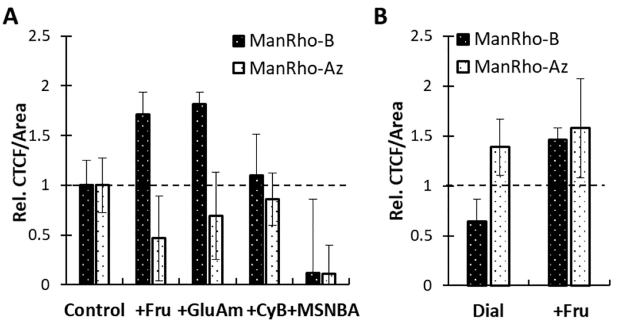

Figure 4. (A) Fluorescence induced by ManRho-B and ManRho-Az (2 μM) in the presence of inhibitors: fructose (Fru, 100 mM), glucosamine (GluAm, 100 mM), cytochalasin B (CyB, 50 μM), and MSNBA (100 μM). Data represent fluorescence derived after quantification of respective fluorescence images using ImageJ as CTCF/area. Relative fluorescence is derived by normalization by the control (probe without inhibitor) − dotted line. Error bars represent the relative standard deviation. A two-tailed *t*-test was used to detect statistically significant differences: *p < 0.05. (B) Impact of fructose preconditioning on ManRho-B and ManRho-Az (2 μM) uptake. Dial: cells cultured in RPMI supplemented with 10% dialyzed FBS; +Fru: cells cultured in RPMI supplemented with 10% dialyzed FBS and 11 mM fructose. Relative fluorescence is derived by normalization of probe-induced fluorescence in preconditioned cell cultures to that of a control culture (dotted line, MCF7 cells cultured in RPMI medium with 10% FBS). Error bars represent the relative standard deviation. Statistically significant differences were established through a two-tailed *t*-test: *p < 0.05.

Specifically, while >80% uptake inhibition by MSNBA reflected GLUT5 involvement in the uptake of both probes, the uptake of ManRho-Az was also inhibited by CyB, reflecting the participation of nonspecific GLUTs. On the contrary, the lack of ManRho-B inhibition by CyB reflected the preferential uptake of this probe through GLUT5. Monitoring the impact of fructose on probes' uptake revealed an intense competition between fructose and ManRho-Az but not ManRho-B. The differences in competition outcomes appear to relate to the differences in the uptake specificities or the lack thereof. For ManRho-B, the lack of competition with fructose can be explained by the 270-fold higher affinity of the probe vs fructose (37 μM vs 10 mM) for GLUT5 and by the ability of fructose to pass through other fructose GLUTs in the presence of a GLUT5 binder.[32] The increase in fructose uptake in the presence of ManRho-B appears to reflect the activation of GLUT5 in the high (100 mM) fructose environment. In contrast, potent inhibition of ManRho-Az uptake by fructose further highlights the nonspecific uptake of the probe, as it reflects the competition for GLUT5 and other fructose GLUTs. The lack of probe uptake inhibition in the presence

https://doi.org/10.1021/cbmi.3c00063
Chem. Biomed. Imaging 2023, 1, 637−647

of GluAm also reflects the GLUT5-specificity of ManRho-B. In contrast, GluAm-induced inhibition of ManRho-Az uptake supports the involvement of GLUT2 in the uptake of this probe. The enhanced levels of ManRho-B uptake in the presence of GluAm appear to reflect the activation of GLUT5 upon inundation of GLUT2 by GluAm.[14]

To assess the GLUT5-ManRho-B relationship and further confirm the differences in the uptake paths for the two probes, we measured the probe-induced fluorescence in MCF7 cells with altered levels of fructose GLUTs. For this part, we relied on the regulatory role of fructose in GLUT5 expression.[33] Preconditioning of Caco2 cells in dialyzed serum and hexose-free medium has been reported to lower expression of GLUT5, and this effect was reversed after fructose and glucose were replenished.[34] A fructose-enriched diet increased GLUT5 levels in the small intestine and kidney of fructose-fed rats.[35] Fructose feeding also contributed to the expression of the GLUT2 transporter, although to a lesser degree than of GLUT5.[35] Accordingly, cells were propagated in the culture medium containing a dialyzed fetal bovine serum (FBS), providing fructose-deprived conditions and fructose-deprived "Dial" culture. In parallel, the dialyzed culture medium was supplemented with 11 mM fructose for establishing a "fructose-fed" MCF7 culture ("+Fru"). MCF7 cells were propagated in the normal complete culture medium to provide the corresponding control. The obtained fructose-fed and fructose-deprived cultures were analyzed for the changes in main fructose transporters GLUT5 and GLUT2, using immunofluorescence staining with the respective GLUT-specific antibodies (Figure S11). The fluorescence analysis highlighted the reduction in GLUT5 levels for the "Dial" culture and some enhancement for GLUT5 in the "+Fru" culture, reflecting the regulatory role of fructose in GLUT5 expression. In contrast to GLUT5, alterations in fructose levels had a stimulating effect on GLUT2 expression regardless of fructose absence or excessive presence.

As summarized in Figures 4B and S12, the uptake of ManRho-B diminished in fructose-deprived "Dial" cultures and increased in fructose-fed "+Fru" cultures. The changes in uptake correlate with the changes in GLUT5 activity and GLUT5 protein levels upon fructose deprivation and fructose feeding, respectively, and highlight the primary involvement of GLUT5 in ManRho-B uptake. On the contrary, an increase in uptake was observed for ManRho-Az regardless of cell culturing conditions, showing a lack of direct correlation with GLUT5 activity and suggesting the involvement of nonspecific fructose uptake paths.

Differences in ManRho Probe Binding Reflect Residues Critical for GLUT5-Specific Uptake

Identifying specific interactions responsible for substrate selection by GLUTs is critical for designing GLUT-targeting probes and inhibitors. To gain a deeper understanding of probe−GLUT5 binding and identify interactions supporting specificity of ManRho-B, we conducted molecular modeling using the outward human homology model of GLUT5 ($GLUT5_{out}$). Human $GLUT5_{out}$ was modeled based on the available crystal structure (PDB:4YBQ).[36]

The molecular docking with $GLUT5_{out}$ positioned the rhodamine residues toward the $GLUT5_{out}$ exit vestibule (Figure 5). Our in silico analysis demonstrated that while both probes were positioned near the fructose-binding site, the sugar moiety of the probes appeared to be displaced from the sugar-binding site. This displacement could potentially be due to the lack of orientational flexibility of the fluorescent moiety of the probe in the rigid protein model.

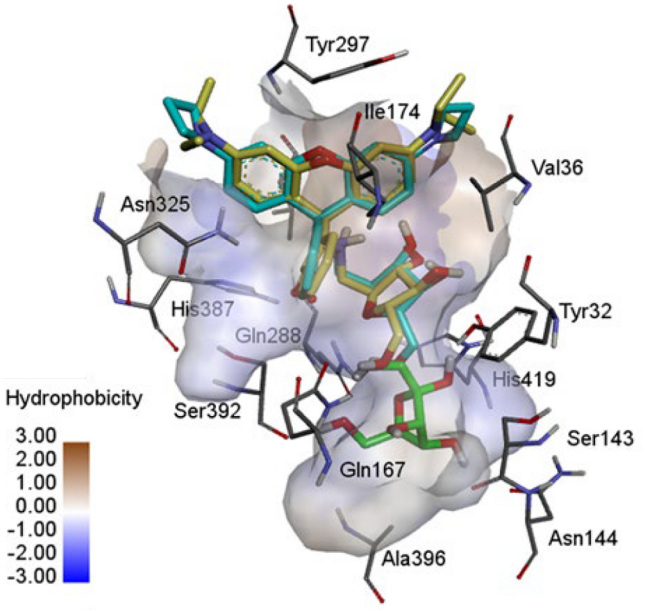

Figure 5. Docked complex of ManRho-B, ManRho-Az, and fructose in the sugar-binding site of outward-facing GLUT5 transporter. The carbons of ManRho-B, ManRho-Az, and fructose are colored yellow, cyan, and green, respectively, and the carbons of protein residues are colored gray. Other atoms are colored as follows: O, red; H, white; N, deep blue. Molecular modeling is visualized in Discovery Studio Visualizer.

The docking analysis resulted in binding scores of −4.7 kcal/mol for ManRho-B and −3.4 kcal/mol for ManRho-Az, indicating that ManRho-B is a better binder. Despite having a similar network of interacted residues, including those important for fructose transport, such as Tyr32, Gln288, His387, and His419,[31] the flexibility of ethyl substituents of ManRho-B (10 vs 6 rotatable bonds in ManRho-Az) may have enabled a better accommodation within the binding pocket and form more favorable interactions with the surrounding residues. Also, the higher lipophilicity of ManRho-B (LogP = 4.66) compared to ManRho-Az (LogP = 4.00) contributes to higher hydrophobic interactions with the isoleucine and valine residues that are located at the opening of the GLUT5.

ManRho Probes Report Differences in Fructose Transport Activity in Cells and In Vivo

Considering the evident preference toward GLUT5-mediated uptake, we evaluated ManRho-B as a comparative reporter of GLUT5 activity in different cells: normal breast 184B5 cells, breast cancer MCF7 and MDA-MB-231 cells, and cervical cancer HeLa cells. For comparative analysis, all cells were treated with ManRho-B solution in a complete cell culture medium for 15 min at 37 °C, and the fluorescence from probe accumulation was analyzed using confocal microscopy and flow cytometry (Figure 6). We observed significant differences in probe fluorescence in four cell lines, and the differences correlated between the two analysis methods. The uptake of ManRho-B was the lowest in normal breast 184B5 cells, in agreement with prior reports.[11,26] Between cancer cells, the highest probe uptake was measured for MCF7 cells, followed by MDA-MB-231 and HeLa.

https://doi.org/10.1021/cbmi.3c00063
Chem. Biomed. Imaging 2023, 1, 637−647

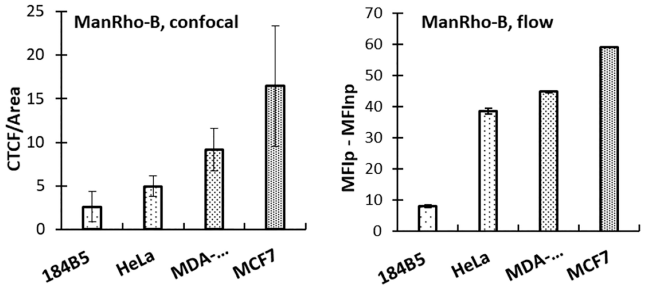

Figure 6. GLUT5 activity screening in live cells treated with ManRho-B (2 μM) using confocal microscopy and flow cytometry. Quantified fluorescence derived from the confocal images (Figure S13) of probe-treated cells using ImageJ as CTCF/area. Flow cytometry analysis of probe-treated cells carried out for 10 000 events, using the YL2 filter of the Attune NxT flow cytometer. The obtained data were processed as MFI_{probe} (median of fluorescence intensity) − $MFI_{noprobe}$ (MFI of the cells with no treatment).

To assess whether the ManRho-B uptake can be reflective of GLUT5 levels in cells, we have performed an immunofluorescence analysis of four cell lines using the GLUT5-specific antibody (Figure S14). The levels of GLUT5 expression were measured to be the lowest for 184B5 cells and the highest for MCF7 cells. HeLa and MDA-MB-231 cells showed an intermediate level of GLUT5 expression. It is notable that the discrepancies in the relative differences between GLUT5 activity and GLUT5 expression may originate from the differences in sensitivity of confocal microscopy and flow cytometry and human error. Nonetheless, the evident correlation between the GLUT5 expression and GLUT5 activity measured with the ManRho-B validated the use of this turn-on fluorescence probe as an analytical tool for GLUT5 activity screening in live cells.

In order to test if the probes can be used at the whole-organism level, we used larvae of *Drosophila melanogaster* as a model.[37,38] *Drosophila* research has made important contributions to elucidating molecular and genetic regulations in larval and adult organs,[39,40] highlighting similarities in sugar-relevant uptake mechanisms and metabolic regulations. For the experiment, first-instar larvae were treated with probes (10 μM) in PBS buffer for 2 h. In parallel, probes were introduced in PBS buffers supplemented with glucose or fructose to assess the potential impact of a nutritional environment on probe accumulation. After 2 h of treatment, larvae were mounted on a glass slide and imaged with a confocal microscope.

The probe-induced fluorescence was well-detectable for both probes in the larval gut (control), although a stronger accumulation was evident for the ManRho-B probe (Figure 7). The differences in probe uptake efficiencies in the larvae correlate with those measured in MCF7 cells, reflecting a lesser uptake for the ManRho-Az analogue. Both probes were accumulated in the presence of glucose (+glucose) or fructose (+fructose), with no alterations in the overall accumulation levels. Compared to glycoconjugates, the aglycone rhodamine B (10 μM) showed a nonspecific distribution within the larvae. (Figure 7). The variances between probe vs aglycone accumulation reflected the differences in the uptake mechanisms between the glycoconjugates and the aglycone, delineating transporter-restricted accumulation of the probes.

Glucose and fructose are sources of carbohydrates for *Drosophila* in nature,[41] suggesting the existence of the corresponding transporters. Feeding larvae with glucose or

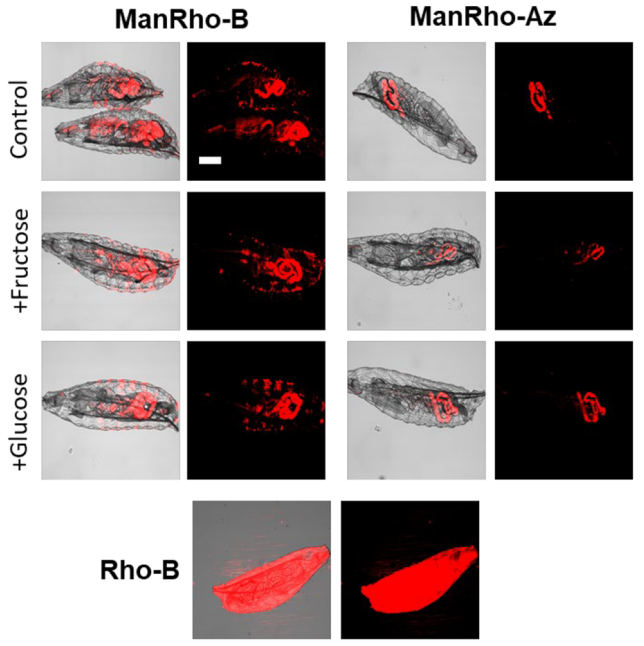

Figure 7. ManRho conjugates vs rhodamine B in *Drosophila melanogaster* larvae after 2 h of treatment. Probes and Rho-B used as 10 μM solutions in a PBS buffer. Control, probes in a PBS buffer containing; +fructose and +glucose, probes in a PBS buffer containing 50 mM fructose or glucose, respectively. Larvae were imaged using a confocal microscope, 10× objective, and an Alexa Fluor 568 filter (exc 559 nm/em 603 nm). All larvae images were taken at the same exposure time. Probe imaging was at 24% laser intensity. Rho-B imaging was at 14% laser intensity. The scale bar is 50 μm.

fructose has been shown to alter metabolic processes and represent an appropriate method for assessing the impacts of sugars.[42] Hence, we assessed the feasibility of the ManRho-B probe to serve as a reporter for alterations in sugar uptake in vivo. For this part, larvae were fed with glucose (glucose+) and fructose (fructose+) for 4 h to alter their nutritional environment. Postfeeding, the larvae were incubated with ManRho-B for 2 h, mounted on slides, and imaged.

After prolonged feeding of the larvae with glucose or fructose, we observed the uptake of the probe to taper off, as compared to the cotreatment ("+glucose" and "+fructose", Figure 8). The existing findings highlight similar effects of high glucose or fructose feeding with respect to diabetes and obesity induction in *Drosophila*.[43] The observed loss in probe accumulation is in agreement with deregulations in sugar uptake upon prolonged high sugar feeding. The differences in site specificity and uptake capability outline the transporter-mediated uptake for ManRho-B, posing it as a tool for monitoring *in vivo* response to alterations in the nutritional environment.

CONCLUSIONS

In conclusion, here we demonstrate the feasibility to deliver larger fluorophores with turn-on properties through GLUTs and present new turn-on fluorescence molecular probes for imaging GLUT activity in live cells and *in vivo*. Through the analysis of uptake profiles for two rhodamine analogues, we reflect a stringent requirement for fluorophore design for maintaining GLUT5-specific delivery. Despite the structural similarities between the two probes, the subtle difference in

https://doi.org/10.1021/cbmi.3c00063
Chem. Biomed. Imaging 2023, 1, 637−647

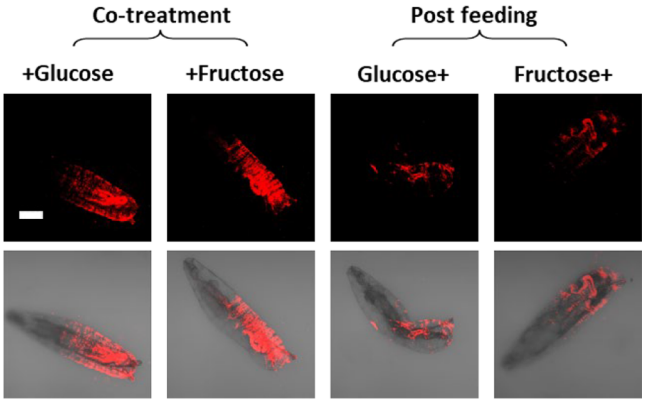

Figure 8. ManRho-B uptake in *Drosophila melanogaster* larvae. +Glucose and +fructose, probe (10 μM) in a PBS buffer supplemented with respective sugar. Larvae treated for 2 h. Glucose + and fructose+ larvae pretreated for 4 h with a PBS buffer containing 50 mM glucose or fructose, respectively, followed by 2 h of probe (10 μM) treatment. Larvae were imaged using a confocal microscope, 10× objective, and Alexa Fluor 568 filter (exc 559 nm/em 603 nm) at the same laser intensity (24%) and exposure time. The scale bar is 50 μm.

amine substitution appears to impact probe uptake efficiency, cellular distribution, and retention. The turn-on fluorescence of the probe allows for eliminating post-treatment steps in cell imaging facilitating real-time monitoring of probe uptake as means of GLUT activity analysis. The responses of the probes to competitive substrates and inhibitors further highlight the applicability of these turn-on reporters for inhibitor screening. Lastly, the efficacy of probe uptake in larvae suggests the potential application of the presented tools for in vivo imaging with continuous image monitoring. Overall, our findings provide a new avenue for designing GLUT-targeting fluorescence probes and show the feasibility of achieving targeted delivery of complex agents *in vitro* and *in vivo*.

EXPERIMENTAL SECTION

Materials and Methods

All reagents were used as received unless otherwise stated from Sigma-Aldrich. Preparative silica chromatography was performed using SiliCycle SiliaFlash F60 40−63 μm (230−400 mesh). Final purification of compounds was achieved with Agilent-1200 HPLC (high-pressure liquid chromatography) using a reversed-phase semipreparative column (Phenomenex Luna 10 μm C18(2) 100 Å, LC Column 100 × 10 mm, Ea). ^{1}H, ^{13}C, and ^{19}F NMR spectra were recorded at room temperature with a Varian Unity Inova 400 MHz spectrometer and a Bruker AVANCE NEO 500 MHz spectrometer. $CDCl_3$ was used as a solvent and referenced to the corresponding residual solvent peaks (7.260 and 77.160 ppm for H- and C NMR, respectively). The following abbreviations are used to indicate the multiplicity: s, singlet; d, doublet; t, triplet; q, quartet; m, multiplet; b, broad signal; app, approximate. The coupling constants are expressed in hertz (Hz). The high-resolution (HR) MS (ESI) spectra were obtained using a Thermo Fisher Orbitrap Elite Hybrid Ion Trap-Orbitrap mass spectrometer at Chemical Advanced Resolution Methods (ChARM) Laboratory at Michigan Technological University. Low-resolution (LR) MS spectra (ESI) were obtained using a Thermo Scientific LCQ Fleet. UV−vis spectra were recorded on a Cary 60 UV−vis spectrophotometer from Agilent Technologies. Fluorescence spectra were obtained with a FluoroMax-4 spectrophotometer.

Normal breast (184B5, ATCC CRL8799), breast cancer (MCF7, ATCC HTB-22 and MDA-MB-231, ATCC CRM-HTB-26), and cervical cancer (HeLa, ATCC CCL-2) cell lines were purchased from the American Type Cell Culture (ATCC, USA). RPMI-1640, dye-free RPMI, DMEM, penicillin/streptomycin, FBS (fetal bovine serum), dialyzed FBS, and 0.25% trypsin−EDTA (1X) were purchased from Life Technologies, USA. Sterile DMSO (25−950-CQC, 250 mL) was purchased from Sigma-Aldrich (St Louis, MO, USA). CellTiter 96 Aqueous One Solution Cell Proliferation Assay was purchased from Promega (Madison, WI, USA). Fructose, glucosamine, and cytochalasin B (CyB) were purchased from Sigma-Aldrich. MSNBA was purchased from MolPort. Lysosensor and MitoView dyes were purchased from Life Technologies, USA, and Biotium, USA, respectively. Mouse monoclonal IgG1 κ Glucose Transporter Glut5 antibody (sc-27105) was purchased from Santa Cruz Biotechnology, USA. Goat anti-Mouse IgG (H+L) Highly Cross-Adsorbed Secondary Antibody, Alexa Fluor Plus 488 (A32723) was purchased from Invitrogen, Thermo Fisher Scientific, USA. Poly-D-lysine-coated 35 mm confocal plates were purchased from MatTek, USA. Cell culture plates treated for increased cell attachment were purchased from VWR, USA. Confocal images were taken with Olympus FluoView FV1000 using the FluoView software. Flow analysis was carried out using Attune NxT flow cytometer.

Synthesis

2,5-Anhydro-2-carbaldehyde-D-mannitol (**3**) was prepared according to the reported procedures.[13] Other compounds were synthesized as outlined below.

2-Amino-3′,6′-bis(diethylamino)spiro[isoindole-3,9′-xanthene]-1-one (Rho-B hydrazine, 1). To a stirred solution of rhodamine B (0.48 g, 1 mmol) in EtOH (20 mL) at room temperature was added an excess of hydrazine hydrate (98%, 1.8 mL, 36.9 equiv) dropwise, and the mixture was heated at reflux for 18 h. Over this time, the fluorescent dark pink solution changed from to transparent orange, and fluorescence disappeared, suggesting the formation of a nonfluorescent spirocyclic structure. After cooling to room temperature, the solvent was removed under reduced pressure. The remained residue was dissolved in $CHCl_3$ (30 mL), and the excess hydrazine hydrate was removed by washing with acid (1 M HCl). The organic phase was neutralized with 1 M NaOH (pH 8−9). The resulting precipitate of **1** was filtered, washed three times with water, and dried in the oven (∼110 °C). Rhodamine B hydrazide (**1**) was obtained in 87% yield as a purple solid. HRMS (ESI): $[M + H]^+$ calcd 456.25253; obsd 457.25776. ^{1}H NMR (500 MHz, $CDCl_3$): δ, 7.93−7.94 (m, 1H), 7.44−7.46 (m, 2H), 7.10−7.11 (m, 1H), 6.45−6.47 (d, 2H, J = 10), 6.42 (d, 2H, J = 2.6), 6.28−6.30 (dd, 2H, J_1 = 2.6, J_2 = 8.9), 3.32−3.36 (q, 8H, J = 7.1), 3.61 (s, 2H), 1.15−1.18 (t, 12H, J = 7.1). ^{13}C NMR (125 MHz, $CDCl_3$): δ, 166.14, 153.85, 151.56, 148.89, 132.50, 130.04, 128.11, 128.10, 123.83, 122.99, 108.04, 104.58, 97.98, 65.92, 44.38, 12.62.

2-Amino-3′,6′-di(azetidine-1-yl)spiro[isoindoline-1,9′′-xanthen]-3-one (Rho-Az hydrazine, 2). To a stirred solution of **B** (0.17 g, 1 equiv, see SI for synthetic details) in EtOH (50 mL) at rt was added hydrazine monohydrate (98%, 0.35 mL, 15 equiv). The mixture was heated at reflux for 18 h. The bright fluorescent solution turned into an inflorescent one overnight. After cooling to rt, the solvent was evaporated under reduced pressure. The solid was dissolved in $CHCl_3$ (10 mL), and the organic phase was washed with H_2O (2 × 10 mL). After the removal of the solvent, product **2** was obtained as a brown-purple solid (90%). LRMS (ESI): m/z $[M + H]^+$ calcd 425.20; obsd 425.33. ^{1}H NMR (400 MHz, $CDCl_3$): δ 7.95−7.91 (m, 1H), 7.47−7.43 (m, 2H), 7.08−7.04 (m, 1H), 6.46 (d, J = 8.5 Hz, 2H), 6.19 (d, J = 2.3 Hz, 2H), 6.06 (dd, J = 8.5, 2.3 Hz, 2H), 3.88 (t, J = 7.2 Hz, 8H), 3.60 (s, 2H), 2.36 (p, J = 7.2 Hz, 4H). ^{13}C NMR (100 MHz, $CDCl_3$): δ 166.26, 153.37, 153.10, 151.58, 132.75, 130.02, 129.48, 128.40, 128.08, 123.90, 123.21, 107.88, 106.75, 98.21, 52.39, 17.04.

Synthesis of Glycoconjugates 4 and 5. Aldehyde **3** (up to 3 equiv) and rhodamine hydrazine (**1** or **2**) (1 equiv) were dissolved in MeOH (25 mL) and stirred at 0 °C for 30 min at a pH of 4 (pH adjusted using AcOH). $NaBH_3CN$ (2.4 equiv) was then added in three portions (0.8 equiv) every 30 min. After the last addition, the reaction was brought to room temperature and stirred for 2 h. The

https://doi.org/10.1021/cbmi.3c00063
Chem. Biomed. Imaging 2023, 1, 637−647

reaction mixture was adsorbed on silica (solvent removed under reduced pressure), dry-loaded onto the silica gel column, and purified by column chromatography. Exclusively for analytical purposes, the final purification was achieved by semipreparative HPLC to obtain the product as light pink solid (5 mg sample).

3′,6′-Bis(diethylamino)-2-((((2*S*,3*R*,4*R*,5*S*)-3,4-dihydroxy-5-(hydroxymethyl)tetrahydrofuran-2-yl)methyl)amino)spiro-[isoindoline-1,9′-xanthen]-3-one (ManRho-B, 4). ManRho-B was eluted using 5% MeOH in CH_2Cl_2 and obtained as a colored solid in 25% yield. HRMS (ESI): m/z $[M + H]^+$ calcd 603.31826; obsd 603.31626. ^{1}H NMR (500 MHz, $CDCl_3$): δ, 7.44−7.48 (m, 2H), 7.86−7.88 (m, 1H), 7.08−7.10 (m, 1H), 6.38−6.43 (m, 4H), 6.26−6.28 (dd, 2H, J_1 = 2.6, J_2 = 8.9), 4.05−4.07 (t, 1H, J = 5), 3.91−3.93 (t, 1H, J = 5), 3.82−3.84 (q, 1H, J = 4), 3.76−3.79 (q, 1H, J = 5), 3.63−3.70 (m, 2H), 3.30−3.35 (q, 8H, J = 7.1), 3.46 (s, 1H), 2.66−2.82 (dABq, 2H, J_{AB} = 45, J_1 = 12.7, J_2 = 6.5), 1.14−1.17 (t, 12H, J = 7.1). ^{13}C NMR (125 MHz, $CDCl_3$): δ,167.11, 153.89, 151.51, 148.75, 132.99, 129.76, 128.57, 128.33, 123.94, 123.01, 108.15, 104.39, 97.93, 84.19, 82.38, 80.90, 78.34, 66.28, 44.38, 29.71, 12.60.

3′,6′-Di(azetidin-1-yl)-2-((((2*S*,3*R*,4*R*,5*S*)-3,4-dihydroxy-5-(hydroxymethyl)tetrahydrofuran-2-yl)methyl)amino)spiro-[isoindoline-1,9′-xanthen]-3-one (ManRho-Az, 5). Purification by silica gel chromatography (3−5% MeOH (2 M NH_3)/CH_2Cl_2, linear gradient) afforded **5** as a pink solid in 20% yield. HRMS (ESI): $[M + H]^+$ calcd 571.25566; obsd 571.25380. ^{1}H NMR (400 MHz, $CDCl_3$): δ 7.92−7.88 (m, 1H), 7.53−7.45 (m, 2H), 7.09−7.05 (m, 1H), 6.42 (dd, J = 8.5, 1.4 Hz, 2H), 6.19 (dd, J = 3.3, 2.3 Hz, 2H), 6.08−6.01 (m, 2H), 4.01 (t, J = 3.9 Hz, 1H), 3.93−3.83 (m, 10H), 3.83−3.74 (m, 2H), 3.74−3.61 (m, 2H), 3.49 (s, 1H), 3.00−2.91 (m, 1H), 2.59 (dd, J = 12.6, 3.7 Hz, 1H), 2.41−2.32 (m, 5H)., 1H), 2.59 (dd, J = 12.6, 3.7 Hz, 1H), 2.41−2.32 (m, 5H). ^{13}C NMR (100 MHz, $CDCl_3$): δ 166.93, 153.40, 153.18, 153.06, 153.00, 151.40, 133.18, 128.59, 128.54, 128.43, 124.00, 123.16, 107.81, 107.75, 106.89, 106.48, 97.94, 85.16, 83.43, 81.57, 79.08, 77.36, 66.13, 63.34, 52.26, 16.93.

Probes and Solutions

For all biological studies, probes of analytical purity were obtained by reverse-phase HPLC purification and were used to prepare a 5 mM stock solution in DMSO. For cell treatments, probe solutions were prepared in the complete cell medium using the stock solution. DMSO concentration was kept below 10%.

Fluorescence and Quantum Yield Measurements

Five millimolar DMSO stock solutions of ManRho-B and ManRho-Az were used to prepare a series of 10 μM solutions of the probe in aqueous pH buffers (pH = 0.8−10). The total volume prepared is 1 or 5 mL. The following aqueous buffer systems were used:[44] pH = 0.8−1.6: HCl/KCl; pH = 3.0−7.0: citric acid/Na_2HPO_4; pH = 8.0−9.0: HCl/Tris; pH = 10: $NaHCO_3/Na_2CO_3$. The absorption spectra of these solutions were recorded using a Cary 60 UV−vis spectrophotometer. The fluorescence spectra (exc 500 nm) of these solutions were measured using a Fluoromax-4 spectrophotometer. Plots of the fluorescence intensity versus pH and the fluorescence versus pH were fitted using a nonlinear curve-fitting technique (GraphPad Prism 9.4.1.) to obtain the pK_a values. All the measurements were carried out at ambient temperature.

Quantum yields (Φ_x) were determined from the absorbance and the integrated fluorescence emission between 520 and 750 nm (excitation at 500 nm) using fluorescein as the fluorescence standard according to the equation below.[45] An excitation and an emission slit width of 5 nm were used. The fluorescence spectra of both the probes and the standard sample were obtained under identical conditions. For each compound, six data points were acquired with absorbances ranging between 0.0025 and 0.1 (l = 10 mm). The Φ_x value was calculated using eq 1, where the subscripts ST and x denote standard and test, respectively, Φ is the fluorescence quantum yield, Grad is the gradient from the plot of integrated fluorescence intensity vs absorbance, and η is the refractive index of the solvent.

$$\Phi_x = \Phi_{ST}\left(\frac{\mathrm{Grad}_x}{\mathrm{Grad}_{ST}}\right)\left(\frac{\eta_x^2}{\eta_{ST}^2}\right) \quad (1)$$

Cell Culture and Plate Preparation

All cultures were supplemented with 10% fetal bovine serum (FBS), 10 000 IU/mL penicillin, and 10 000 μg/mL streptomycin to lower the chances of bacterial contamination. The MCF7 and MDA-MB-231 cell lines were cultured using RPMI-1640. Fructose-reconditioned (Dial) cells were obtained by propagating MCF7 cells in RPMI, supplemented with dialyzed FBS (10%), and 1% penicillin/streptomycin for 14 days. Fructose-supplemented (+Fru) cells were obtained by propagating MCF7 cells in RPMI, supplemented with dialyzed FBS (10%), 1% penicillin/streptomycin, and 11 mM fructose for 14 days. HeLa cells were grown and maintained using a DMEM medium supplemented with FBS (10%) and 1% penicillin/streptomycin. Cells were collected at ∼80% confluence of the 10 mm tissue culture plate using 0.25% trypsin−EDTA (2 mL). The trypsin fraction was diluted with culture medium to 5 mL, and cells were pelleted by centrifugation (1600 rpm, 5 min), reconstituted in the complete culture medium (5 mL), and plated with a desired seeding density. The total volume in the wells was brought to the desired volume by the corresponding medium. After 12 h, the culture medium was changed, and cells were allowed to grow for 48 h from the moment of cultivation. All cells were maintained at 37 °C, at 65% relative humidity, and under 5% CO_2 in the ATCC-suggested respective culture mediums and subcultures according to the ATCC protocol. Cells were seeded in 10 cm cell culture dishes treated for increased cell attachment. All experiments were carried out with cells in passages 15−25.

Fluorescence Confocal Imaging

Cells were pelleted by centrifugation, reconstituted in the complete culture medium (5 mL), and plated with a seeding density of 150 000 cells per 35 mm glass-bottom confocal dishes (MatTek). The total volume in the plate was brought to 2 mL by the corresponding medium when needed. Cells were maintained at 37 °C in 5% CO_2 for 12 h. After 12 h, the culture medium was changed, and cells were allowed to grow for 48 h from the moment of cultivation.

After 48 h, the cell medium was removed, and a treatment solution (2 mL) was added. Cells were incubated with probes at 37 °C for a specific time interval. For "no wash" conditions, cells were imaged directly after incubation. For "wash" conditions, after incubation, the probe solution was removed, and cells were washed with complete culture media (2 × 1 mL) and replenished with 2 mL of medium for imaging.

Images were taken with Olympus FluoView FV1000 using the FluoView software. A 60× oil-suspended lens was used to observe fluorescent activity with the following conditions: Alexa 568, laser 559 nm, 20 μs/pixel. The obtained fluorescence images were quantified using ImageJ. Fluorescence was calculated as corrected total cell fluorescence (CTCF) (CTCF = integrated density − (area of selected cell × mean fluorescence of background readings).[48] CTCF was normalized by the area of the selected cell (CTCF/area of the selected cell). This procedure was done for cells by selecting regions of interest in the single image. The finalized values represent an average fluorescence of 7−15 cells per image. At least two images per sample were processed.

First-instar larvae of the *Drosophila melanogaster* wild-type stock Canton-S were collected after hatching from the eggs, washed 2× in PBS solution, and incubated in 400 μL of a PBS-based probe solution (with and without sugar solutions added) for 2 h. After the incubation, the larvae were washed 3× in PBS, mounted alive on slides, and covered with a coverslip. Fluorescence imaging was performed with a confocal fluorescence microscope (Olympus) using a 10× objective lens. An Alexa Fluor 568 filter (exc 559 nm/em 603 nm) was used. All images were taken at the same exposure time.

https://doi.org/10.1021/cbmi.3c00063
Chem. Biomed. Imaging 2023, 1, 637−647

Colocalization Analysis

Intracellular localization of the ManRho probes was performed using MitoView and Lysosensor Green in MCF7 cells. Confocal dishes were plated with a seeding density of 150 000 cells per 35 mm glass-bottom confocal dishes (MatTek) and incubated at 37 °C for 48 h. For the ManRho and MitoView costain, a solution of ManRho (2 μM) and MitoView (1 μM) in cell media was added and cells were incubated at 37 °C for 15 min. For the ManRho and Lysosensor costain, a solution of ManRho (2 μM) and Lysosensor Green (1 μM) in cell media was added to cells and incubated at 37 °C for 15 min. Confocal fluorescence imaging studies were performed with a confocal microscope with a 60× objective lens. Image analysis was done using ImageJ. The Pearson's correlation coefficient was calculated using the Colocalization Finder ImageJ plugin.[46]

Concentration-Dependent Uptake

Probe solutions (1, 5, 10, 25, 50, 75, 100, 200, and 500 μM) were prepared in 2 mL of complete cell medium using the stock solution. DMSO concentration was kept below 10%. MCF7 cells seeded in glass-bottom confocal dishes or six-well plates were used for treatment. The cell medium was removed, and a probe solution (2 mL) was added. The cells were incubated with probes at 37 °C for 15 min. After incubation, the probe solution was removed, and the cells were washed with complete culture media (2 × 1 mL) and replenished with 2 mL of medium for analysis, using confocal microscopy or flow cytometry.

Efflux Studies

MCF7 cells seeded in confocal plates were treated with probe solution (2 μM) and incubated at 37 °C and 5% CO_2 for 15 min. After the incubation, the probe solution was discarded. The cells were replenished with fresh dye-free medium (2 mL) and incubated at 37 °C and 5% CO_2 for 5 and 20 min. The medium was then collected and centrifuged for 3 min at 3000 rpm to sediment floaters and debris. The supernatant was transferred into a new tube, and the fluorescence of the dye-free medium was measured using a Fluoromax-4 spectrophotometer.

Temperature Studies

MCF7 cells were seeded in confocal plates. Before treatment with probes, confocal plates with the seeded cells were kept in the refrigerator at ∼4 °C for 30 min. After that, the culture medium was discarded, and a cooled solution of a probe in complete the culture medium was added. Cells were kept in the refrigerator for 15 min. After treatment, the probe solution was removed, and the cells were washed with culture medium (2 × 1 mL) and replenished with 2 mL of medium for imaging.

Competitive Uptake Inhibition

The following stock solutions were used: fructose and glucosamine (200 mM in complete culture medium), MSNBA (5 mM in DMSO), and CyB (500 μM in DMSO). For treatment, stock solutions of inhibitors were diluted with complete culture medium to reach the 2× of required concentration and further diluted by the probe-containing solution to reach the targeted inhibitor concentration. MCF7 cells seeded in glass-bottom confocal dishes were used. Cell culture medium was removed, and a probe + inhibitor containing culture media solution (2 mL) was added. Cells were incubated at 37 °C for 15 min. After the incubation, the probe + inhibitor solution was removed, and the cells were washed with a complete culture medium (2 × 1 mL) and replenished with 2 mL of medium for fluorescence imaging. Cells treated with a 2 μM ManRho probe were used as a control.

GLUT5 Immunofluorescence Analysis

Cells were grown in their respective media and harvested using 0.25% trypsin. After the centrifugation, trypsin was discarded, and the cells were reconstituted in a complete growth medium, seeded in confocal dishes, and allowed to adhere for 12 h. Then, the cells were fixed with 4% PFA for 20 min, followed by washes with PBS (3 × 2 mL) for a total of 15 min. The cells were then protein-blocked using bovine serum albumin, followed by overnight incubation at 4 °C with the primary antibody (Santa Cruz Biotechnology, sc-27105) at a dilution of 1:200. Next, the cells were washed with PBS (2 × 2 mL) and incubated for 2 h with the secondary antibody conjugated to Alexa 488 (Invitrogen, Thermo Fisher Scientific, A32723) at a dilution of 1:1000. After the reagents were washed off, the cells were imaged using a confocal microscope, a 60× objective, and an Alexa 488 filter.

Fluorescence Analysis Using Flow Cytometry

Flow-based analysis was carried out in parallel with the confocal analysis with cells seeded in six-well plates. For this part, the cell medium was removed, and cells were treated with the probe solution (2 mL) and incubated with probes at 37 °C at 5% CO_2 for 15 min. After the incubation, the probe solution was removed, and the cells were detached from the plate using trypsin (0.5 mL). The trypsin fraction was diluted with a culture medium to 1 mL and transferred into a microcentrifuge tube (1.5 mL) for cell fluorescence analysis by flow cytometry. Fluorescence data of 10 000 events were obtained, using the YL2 filter of the Attune NxT flow cytometer. The obtained data were processed as MFI_{probe} (median of fluorescence intensity) − $MFI_{noprobe}$ (MFI of the cells with no treatment). MFI was derived excluding debris and doublets by FSC-SSC and FSC-H-FSC-W gating, respectively.

Cytotoxicity Studies

The MCF7 cell pellet, obtained as described within plate preparation, was reconstituted in the complete RPMI medium, seeded in 96-well flat-bottom opaque walled plates (10 000 cells/well), and allowed to grow for 24 h at 37 °C and 5% CO_2. At the end of 24 h, the medium was discarded, and the cells were replenished with medium supplemented with a ManRho probe (concentrations varying from 0 to 200 μM) and incubated at 37 °C and 5% CO_2 for 24 h. Then, 20 μL of the CellTiter96 Aqueous One solution of the cell proliferation assay kit (Promega-G3582) was added directly to each well, and the cells were incubated for 4 h at 37 °C and 5% CO_2. Wells with medium only were used as the negative control. Untreated cells represent 100% of cell viability. After the 4 h incubation, the absorbance was immediately recorded using an automated UV 96-well plate reader at 490 nm wavelength. Cell viability of treated cells was calculated as a relative decrease in the absorbance with respect to the untreated control: viability, % = $(A_{treatment} - A_{control}) \times 100$ (where A = absorbance). The results represent the mean ± SD of triplicate samples.

Molecular Modeling

Energy minimization of the analyzed proteins was performed using YASAR online server.[47] The structures of ManRho-B and ManRho-Az were drawn in ChemDraw 20.1.1. The energies of all ligands were minimized in Avogadro.[48,49] Gasteiger charges were added to ligand/protein structures. AutoDockTools (ADT) version 1.5.6[50,51] was used to add Gasteiger charges and polar hydrogens and prepare the ligand and protein for further docking in AutoDockVina.[52] Docking in AutoDockVina was performed with default parameters using pdbqt files of protein and ligand as input. The visualization of docked complexes was carried out in DS Visualizer.

Quantification, Statistical, and Kinetic Analysis

Quantified fluorescence is reported as CTCF/cell area. Data are presented as ± standard deviation of the average fluorescence (calculated by Excel) between cells in two independent experiments. Graphs were built in Microsoft Excel. The relative fluorescence was derived by dividing the average fluorescence (control or sample) by that of the control. Relative standard deviation is derived by dividing the individual standard deviation by the average standard deviation. Statistical significance was calculated using a two-tailed t-test and is indicated in the figures using the following denotation: $*p < 0.05$. The probe uptake kinetic analysis was carried out using enzyme kinetic velocity as a function of the substrate model. pK_a values were derived using nonlinear regression analysis. All calculations were performed using GraphPad Prism 9.4.1.

https://doi.org/10.1021/cbmi.3c00063
Chem. Biomed. Imaging 2023, 1, 637−647

■ ASSOCIATED CONTENT

Supporting Information

The Supporting Information is available free of charge at https://pubs.acs.org/doi/10.1021/cbmi.3c00063.

Data figures, tables, graphs, cell images, procedures, methods, synthetic details, and ^{1}H, ^{13}C, and ^{19}F NMR spectra for all compounds (PDF)

■ AUTHOR INFORMATION

Corresponding Author

Marina Tanasova − *Department of Chemistry and Health Research Institute, Michigan Technological University, Houghton, Michigan 49931, United States;* orcid.org/0000-0003-4771-9533; Email: mtanasov@mtu.edu

Authors

Monica Mame Soma Nyansa − *Department of Chemistry, Michigan Technological University, Houghton, Michigan 49931, United States;* orcid.org/0000-0002-2326-9569

Adelina Oronova − *Department of Chemistry and Health Research Institute, Michigan Technological University, Houghton, Michigan 49931, United States;* orcid.org/0000-0002-4918-5013

Nazar Gora − *Department of Chemistry and Health Research Institute, Michigan Technological University, Houghton, Michigan 49931, United States;* orcid.org/0000-0003-0589-8799

Micaela Rayne Geborkoff − *Department of Biological Sciences, Michigan Technological University, Houghton, Michigan 49931, United States*

Nathan Randal Ostlund − *Department of Biological Sciences, Michigan Technological University, Houghton, Michigan 49931, United States*

Delaney Raine Fritz − *Department of Biological Sciences, Michigan Technological University, Houghton, Michigan 49931, United States*

Thomas Werner − *Department of Biological Sciences and Health Research Institute, Michigan Technological University, Houghton, Michigan 49931, United States*

Complete contact information is available at: https://pubs.acs.org/10.1021/cbmi.3c00063

Author Contributions

M.N. and A.O. contributed equally to probe synthesis, characterization, experimental evaluation in mammalian cells, data analysis, and manuscript writing. N.G. and A.O. performed immunofluorescence analysis. N.G. carried out molecular modeling. M.R.G, N.R.O, D.R.F, and T.W. performed the in vivo studies. M.T. conceptualized and supervised the studies. M.T., A.O., and M.N. wrote the manuscript. N.G. and T.W. edited the manuscript.

Author Contributions

‖Equal contribution as co-first authors.

Notes

The authors declare no competing financial interest.

■ ACKNOWLEDGMENTS

This research was supported by the NIH-R15-AREA (GRANT12736422) award to M. Tanasova.

■ REFERENCES

(1) Wright, E. M.; Hirayama, B. A.; Loo, D. F. Active sugar transport in health and disease. *J. Int. Med.* **2007**, *261*, 32−43.

(2) Ismail, A.; Tanasova, M. Importance of GLUT Transporters in Disease Diagnosis and Treatment. *Int. J. Mol. Sci.* **2022**, *23*, 8698.

(3) Vaupel, P.; Multhoff, G. Revisiting the Warburg effect: historical dogma versus current understanding. *J. Physiol.* **2021**, *599*, 1745−1757.

(4) Szablewski, L. Glucose transporters as markers of diagnosis and prognosis in cancer diseases. *Oncol. Rev.* **2022**, *16*, 561.

(5) Tanasova, M.; Begoyan, V. V.; Weselinski, L. J. Targeting Sugar Uptake and Metabolism for Cancer Identification and Therapy: An Overview. *Curr. Top. Med. Chem.* **2018**, *18*, 467−483.

(6) Nakagawa, T.; Lanaspa, M. A.; Millan, I. S.; Fini, M.; Rivard, C. J.; Sanchez-Lozada, L. G.; Andres-Hernando, A.; Tolan, D. R.; Johnson, R. J. Fructose contributes to the Warburg effect for cancer growth. *Cancer Metab.* **2020**, *8*, 16.

(7) Kumar, P.; Shustov, G.; Liang, H.; Khlebnikov, V.; Zheng, W. Z.; Yang, X. H.; Cheeseman, C.; Wiebe, L. I. Design, Synthesis, and Preliminary Biological Evaluation of 6-O-Glucose-Azomycin Adducts for Diagnosis and Therapy of Hypoxic Tumors. *J. Med. Chem.* **2012**, *55*, 6033−6046.

(8) Wuest, M.; Hamann, I.; Bouvet, V.; Glubrecht, D.; Marshall, A.; Trayner, B.; Soueidan, O. M.; Krys, D.; Wagner, M.; Cheeseman, C.; West, F.; Wuest, F. Molecular Imaging of GLUT1 and GLUT5 in Breast Cancer: A Multitracer Positron Emission Tomography Imaging Study in Mice. *Mol. Pharmacol.* **2018**, *93*, 79−89.

(9) Niu, B.; Wen, X. A.; Jia, Z. J.; Wu, X. M.; Guo, W. H.; Sun, H. B. Synthesis and Preliminary Evaluation of 1-[F-18]Fluoro-1-deoxy-2,5-anhydro-D-mannitol as a PET Radiotracer for Breast Cancer Imaging. *Chin. J. Chem.* **2013**, *31*, 1159−1163.

(10) Oronova, A.; Tanasova, M. Late-Stage Functionalization through Click Chemistry Provides GLUT5-Targeting Glycoconjugate as a Potential PET Imaging Probe. *Int. J. Mol. Sci.* **2023**, *24*, 173.

(11) Nahrjou, N.; Ghosh, A.; Tanasova, M. Targeting of GLUT5 for Transporter-Mediated Drug-Delivery Is Contingent upon Substrate Hydrophilicity. *Int. J. Mol. Sci.* **2021**, *22*, 5073.

(12) Wlodarczyk, J.; Wlodarczyk, M.; Zielinska, M.; Jedrzejczak, B.; Dziki, L.; Fichna, J. Blockade of fructose transporter protein GLUT5 inhibits proliferation of colon cancer cells: proof of concept for a new class of anti-tumor therapeutics. *Pharmacol. Rep.* **2021**, *73*, 939−945.

(13) Yang, J.; Dowden, J.; Tatibouet, A.; Hatanaka, Y.; Holman, G. D. Development of high-affinity ligands and photoaffinity labels for the D-fructose transporter GLUT5. *Biochem. J.* **2002**, *367*, 533−9.

(14) Begoyan, V. V.; Weselinski, L. J.; Xia, S.; Fedie, J.; Kannan, S.; Ferrier, A.; Rao, S.; Tanasova, M. Multicolor GLUT5-permeable fluorescent probes for fructose transport analysis. *Chem. Commun.* **2018**, *54*, 3855−3858.

(15) Levi, J.; Cheng, Z.; Gheysens, O.; Patel, M.; Chan, C. T.; Wang, Y. B.; Namavari, M.; Gambhir, S. S. Fluorescent fructose derivatives for imaging breast cancer cells. *Bioconjugate Chem.* **2007**, *18*, 628−634.

(16) Rana, N.; Aziz, M. A.; Oraby, A. K.; Wuest, M.; Dufour, J.; Abouzid, K. A. M.; Wuest, F.; West, F. G. Towards Selective Binding to the GLUT5 Transporter: Synthesis, Molecular Dynamics and In Vitro Evaluation of Novel C-3-Modified 2,5-Anhydro-D-mannitol Analogs. *Pharmaceutics* **2022**, *14*, 828.

(17) Kannan, S.; Begoyan, V. V.; Fedie, J. R.; Xia, S.; Weselinski, L. J.; Tanasova, M.; Rao, S. Metabolism-Driven High-Throughput Cancer Identification with GLUT5-Specific Molecular Probes. *Biosensors* **2018**, *8*, 39.

(18) Yamamoto, T.; Tanaka, S.; Suga, S.; Watanabe, S.; Nagatomo, K.; Sasaki, A.; Nishiuchi, Y.; Teshima, T.; Yamada, K. Syntheses of 2-NBDG analogues for monitoring stereoselective uptake of D-glucose. *Bioorg. Med. Chem. Lett.* **2011**, *21*, 4088−96.

(19) Otsuka, Y.; Sasaki, A.; Teshima, T.; Yamada, K.; Yamamoto, T. Syntheses of D-Glucose Derivatives Emitting Blue Fluorescence through Pd-Catalyzed C-N Coupling. *Org. Lett.* **2016**, *18*, 1338−1341.

(20) Kobayashi, H.; Ogawa, M.; Alford, R.; Choyke, P. L.; Urano, Y. New strategies for fluorescent probe design in medical diagnostic imaging. *Chem. Rev.* **2010**, *110*, 2620−2640.
(21) Chen, X.; Pradhan, T.; Wang, F.; Kim, J. S.; Yoon, J. Fluorescent chemosensors based on spiroring-opening of xanthenes and related derivatives. *Chem. Rev.* **2012**, *112*, 1910−1956.
(22) Stevens, B.; Sharpe, R. R.; Bingham, W. S. W. Ph-Dependence of Rhodamine B Semiquinone Dismutation Rate in Aqueous Alcoholic Solution. *Photochem. Photobiol.* **1967**, *6*, 83−89.
(23) Grimm, J. B.; Tkachuk, A. N.; Xie, L.; Choi, H.; Mohar, B.; Falco, N.; Schaefer, K.; Patel, R.; Zheng, Q.; Liu, Z.; Lippincott-Schwartz, J.; Brown, T. A.; Lavis, L. D. A general method to optimize and functionalize red-shifted rhodamine dyes. *Nat. Methods* **2020**, *17*, 815−821.
(24) Liew, S. S.; Du, S.; Ge, J.; Pan, S.; Jang, S. Y.; Lee, J. S.; Yao, S. Q. A chemoselective cleavable fluorescence turn-ON linker for proteomic studies. *Chem. Commun.* **2017**, *53*, 13332−13335.
(25) Zhou, J.; Lin, X.; Ji, X.; Xu, S.; Liu, C.; Dong, X.; Zhao, W. Azetidine-Containing Heterospirocycles Enhance the Performance of Fluorophores. *Org. Lett.* **2020**, *22*, 4413−4417.
(26) Tanasova, M.; Plutschack, M.; Muroski, M. E.; Sturla, S. J.; Strouse, G. F.; McQuade, D. T. Fluorescent THF-Based Fructose Analogue Exhibits Fructose-Dependent Uptake. *Chembiochem* **2013**, *14*, 1263−1270.
(27) Smith, F. A. Links between Glucose Uptake and Metabolism in Nitella Translucens. *J. Exp. Bot.* **1967**, *18*, 348−358.
(28) Augustin, R. The protein family of glucose transport facilitators: It's not only about glucose after all. *IUBMB Life* **2010**, *62*, 315−333.
(29) Kapoor, K.; Finer-Moore, J. S.; Pedersen, B. P.; Caboni, L.; Waight, A.; Hillig, R. C.; Bringmann, P.; Heisler, I.; Muller, T.; Siebeneicher, H.; Stroud, R. M. Mechanism of inhibition of human glucose transporter GLUT1 is conserved between cytochalasin B and phenylalanine amides. *Proc. Natl. Acad. Sci. U.S.A.* **2016**, *113*, 4711−4716.
(30) George Thompson, A. M.; Ursu, O.; Babkin, P.; Iancu, C. V.; Whang, A.; Oprea, T. I.; Choe, J.-Y. Discovery of a specific inhibitor of human GLUT5 by virtual screening and in vitro transport evaluation. *Sci. Rep.* **2016**, *6*, 24240−24248.
(31) Uldry, M.; Ibberson, M.; Hosokawa, M.; Thorens, B. GLUT2 is a high affinity glucosamine transporter. *FEBS Lett.* **2002**, *524*, 199−203.
(32) Gora, N.; Weselinski, L. J.; Begoyan, V. V.; Cooper, A.; Choe, J. Y.; Tanasova, M. Discrimination of GLUTs by Fructose Isomers Enables Simultaneous Screening of GLUT5 and GLUT2 Activity in Live Cells. *ACS. Chem. Biol.* **2023**, *18*, 1089−1100.
(33) Cui, X. L.; Ananian, C.; Perez, E.; Strenger, A.; Beuve, A. V.; Ferraris, R. P. Role of cAMP in regulating GLUT5 expression in the neonatal rat small intestine. *Faseb J.* **2002**, *16*, A805−A805.
(34) Mesonero, J.; Matosin, M.; Cambier, D.; Rodriguez-Yoldi, M. J.; Brot-Laroche, E. Sugar-dependent expression of the fructose transporter GLUT5 in Caco-2 cells. *Biochem. J.* **1995**, *312* (Pt 3), 757−762.
(35) Burant, C. F.; Saxena, M. Rapid Reversible Substrate Regulation of Fructose Transporter Expression in Rat Small-Intestine and Kidney. *Am. J. Physiol.* **1994**, *267*, G71−G79.
(36) Nomura, N.; Verdon, G.; Kang, H. J.; Shimamura, T.; Nomura, Y.; Sonoda, Y.; Hussien, S. A.; Qureshi, A. A.; Coincon, M.; Sato, Y.; Abe, H.; Nakada-Nakura, Y.; Hino, T.; Arakawa, T.; Kusano-Arai, O.; Iwanari, H.; Murata, T.; Kobayashi, T.; Hamakubo, T.; Kasahara, M.; Iwata, S.; Drew, D. Structure and mechanism of the mammalian fructose transporter GLUT5. *Nature* **2015**, *526*, 397−401.
(37) Wan, S.; Vohs, T.; Steenwinkel, T. E.; White, W. R.; Lara-Ramirez, A.; Luck, R. L.; Werner, T.; Tanasova, M.; Liu, H. Near-Infrared Fluorescent Probes with Amine-Incorporated Xanthene Platforms for the Detection of Hypoxia. *ACS Appl. Bio. Mater.* **2022**, *5*, 4294−4300.
(38) Zhang, Y.; Xia, S.; Wan, S.; Steenwinkel, T. E.; Vohs, T.; Luck, R. L.; Werner, T.; Liu, H. Ratiometric Detection of Glutathione Based on Disulfide Linkage Rupture between a FRET Coumarin Donor and a Rhodamine Acceptor. *Chembiochem* **2021**, *22*, 2282−2291.
(39) Alfa, R. W.; Kim, S. K. Using Drosophila to discover mechanisms underlying type 2 diabetes. *Dis. Model. Mech.* **2016**, *9*, 365−376.
(40) Hafen, E. Cancer, type 2 diabetes, and ageing: news from flies and worms. *Swiss Med. Wkly.* **2004**, *134*, 711−719.
(41) Keller, A. Drosophila melanogaster's history as a human commensal. *Curr. Biol.* **2007**, *17*, R77−R81.
(42) Rovenko, B. M.; Perkhulyn, N. V.; Gospodaryov, D. V.; Sanz, A.; Lushchak, O. V.; Lushchak, V. I. High consumption of fructose rather than glucose promotes a diet-induced obese phenotype in Drosophila melanogaster. *Comp. Biochem. Physiol. A* **2015**, *180*, 75−85.
(43) Musselman, L. P.; Fink, J. L.; Baranski, T. J. Similar effects of high-fructose and high-glucose feeding in a Drosophila model of obesity and diabetes. *PLoS One* **2019**, *14*, No. e0217096.
(44) Millipore Sigma Buffer Reference Center, https://www.sigmaaldrich.com/US/en/technical-documents/protocol/protein-biology/protein-concentration-and-buffer-exchange/buffer-reference-center.
(45) Limited, H. U. A Guide to Recording Fluorescence Quantum Yields, https://static.horiba.com/fileadmin/Horiba/Application/Materials/Material_Research/Quantum_Dots/quantumyieldstrad.pdf.
(46) Laummonerie, C.; Mutterer, J.; Carl, P. Colocalization Finder, https://imagej.nih.gov/ij/plugins/colocalization-finder.html.
(47) Krieger, E.; Joo, K.; Lee, J.; Lee, J.; Raman, S.; Thompson, J.; Tyka, M.; Baker, D.; Karplus, K. Improving physical realism, stereochemistry, and side-chain accuracy in homology modeling: Four approaches that performed well in CASP8. *Proteins* **2009**, *77*, 114−122.
(48) Avogadro: an open-source molecular builder and visualization tool. Version 1.2.0. http://avogadro.cc/.
(49) Hanwell, M. D.; Curtis, D. E.; Lonie, D. C.; Vandermeersch, T.; Zurek, E.; Hutchison, G. R. Avogadro: an advanced semantic chemical editor, visualization, and analysis platform. *J. Cheminform.* **2012**, *4*, 17.
(50) Sanner, M. F. Python: a programming language for software integration and development. *J. Mol. Graph. Model.* **1999**, *17*, 57−61.
(51) Morris, G. M.; Huey, R.; Lindstrom, W.; Sanner, M. F.; Belew, R. K.; Goodsell, D. S.; Olson, A. J. AutoDock4 and AutoDockTools4: Automated docking with selective receptor flexibility. *J. Comput. Chem.* **2009**, *30*, 2785−2791.
(52) Trott, O.; Olson, A. J. AutoDock Vina: Improving the speed and accuracy of docking with a new scoring function, efficient optimization, and multithreading. *J. Comput. Chem.* **2009**, *31*, 455−461.

https://doi.org/10.1021/cbmi.3c00063
Chem. Biomed. Imaging 2023, 1, 637−647